ELSEVIER

Applied Mathematical Modelling 24 (2000) 795–805

APPLIED MATHEMATICAL MODELLING

www.elsevier.nl/locate/apm

A hybrid method for simulation of axial flow impeller driven mixing vessels

H.M. Blackburn *, J.R. Elston, D.A. Niclasen, M. Rudman, J. Wu

CSIRO Building, Construction and Engineering, P.O. Box 56, Highett, Victoria 3190, Australia

Received 8 March 1999; received in revised form 17 February 2000; accepted 7 March 2000

Abstract

A hybrid method for the simulation of Reynolds-averaged turbulent flows in axial flow impeller driven mixing vessels is described. The time-mean flow in the impeller region is modelled using blade element theory, while the flow in the remainder of the vessel is simulated using a second-order finite-volume Reynolds-averaged numerical scheme. The two models are iteratively coupled through boundary conditions and computation of the power dissipated in the mixing vessel. This approach is computationally cheaper than alternatives that require the details of the flow in the impeller region to be resolved. Simulation results are compared to a detailed laser-Doppler examination of the flow in a laboratory vessel, and it is shown that the average absolute difference between simulated and measured velocities was of the order of 1% of the impeller tip speed. In addition the power consumption was predicted to two-figure accuracy.

Keywords: Mixing; Impeller; Blade element; Simulation

1. Introduction

Impeller-driven mixing vessels are used extensively throughout the process industries, but in the absence of a simplified understanding both of the global flows in the tanks and in the impeller region, design optimisation has been difficult to achieve. Simulation of tank flows is an alternative to experimental studies and is particularly suited to flow optimisation. However, simulation is impeded by the fact that accurate representation of flows in the impeller region is computationally expensive, even if the flows are treated as steady in both the impeller and tank sub-domains [5].

In response to these problems we have developed a hybrid simulation scheme for mixing tanks driven by axial flow impellers. The mean flow in the impeller region is calculated using a blade element approach [8] while the flow in the tank is predicted using a finite-volume Reynolds-averaged Navier–Stokes (RANS) simulation code. The two sets of calculations are coupled via their respective boundary conditions in an iterative scheme. The operating point is set by matching the estimated impeller shaft power to the estimated turbulent power dissipation in the tank fluid. As a result of simplifying the treatment of flows within the impeller region, the

* Corresponding author. Tel.: +61-3-9252-6330; fax: +61-3-9252-6240.
E-mail address: hugh.blackburn@dbce.csiro.au (H.M. Blackburn).

0307-904X/00/$ - see front matter
PII: S0307-904X(00)00019-6

requirements of the complete simulation are sufficiently modest that realistic solutions can be obtained using workstation-level resources.

In earlier work [7], a blade element approach was also adopted for use with axial flow impellers. In that method, the impeller region was included in the computational domain, and blade element theory was used to calculate momentum source terms for cells within the region. Our technique uses a different approach, in part because of a desire to support and augment a separate strand of research that deals with simplified blade element models for tank-impeller flows with non-Newtonian rheologies.

The computational technique described here has also been supported by a laboratory programme of experimental measurements in mixing tanks in which the mean and standard deviation velocity fields have been measured using laser-Doppler velocimetry (LDV). This has enabled us to obtain extensive validation data and to supplement the computational model where required (e.g., for the estimation of turbulence properties on the impeller outflow).

2. Equipment

The mixing rig consisted of a 390 mm diameter circular cylindrical acrylic tank with a flat bottom that was positioned within a square outer glass tank filled with water in order to minimise optical distortion. Four vertical 12.5 mm wide, flat plate baffles were sealed to the tank walls at equal spacings around the periphery of the tank. A Lightnin A310 193 mm diameter 3-blade stainless steel impeller was located on a 25 mm diameter shaft at the centre of the tank and suspended from a frame located above the tank. The shaft penetrated the full depth of the tank, which was filled with water to a depth of 400 mm and the mid-plane of the impeller was 120 mm above the bottom of the tank, arranged so as to pump towards the bottom of the tank. With a rotational speed of 300 rpm the Reynolds number $Re = \pi ND^2/2\nu = 3 \times 10^6$ where N is the rotational frequency, D the impeller diameter and ν the kinematic viscosity.

A sketch of the measurement system employed is shown in Fig. 1. An Ono–Soki torque transducer was used to measure shaft torque and an opto-electronic speed detector was used to

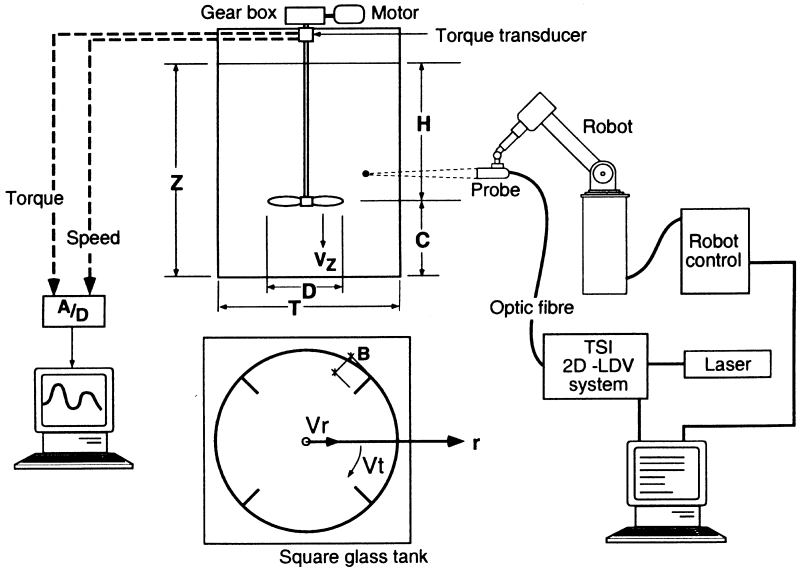

Fig. 1. Layout of two-component LDV measurement system.

measure rotational speed. Transducer signals were logged on a data-collection computer. A TSI 2D-LDV system with a GMFanuc-Robotics S-10 robot traversing system was used to obtain measurements of mean and fluctuating velocity components in the axial, radial and azimuthal directions at specified locations within the tank.

3. Modelling

In this section we outline the theoretical and computational techniques used predict flows in the impeller and tank, and the coupling of the two models.

3.1. Blade element theory

The arbitrary-vortex axial flow blade element theory we use has been previously described in [3]; here the core equations are given without detailed derivation. A sketch of the impeller and the velocity vector diagrams for an element of blade with chord c, at radius r, radial length dr are shown in Fig. 2. It is assumed that radial flows within the impeller volume are negligible.

3.1.1. Flow at each blade element

The velocities at blade inlet (denoted by subscript 1) and outlet (denoted by subscript 2) include the absolute velocity V observed in the fixed frame of reference, the relative velocity W observed in the rotating frame of reference and the impeller velocity $U = 2\pi Nr$. The lift and drag forces are calculated using a mean relative velocity

$$W_{\mathrm{m}} = \left[\left(\frac{(V_{\mathrm{a1}} + V_{\mathrm{a2}}}{2} \right)^2 + \left(U - \frac{V_{\theta 1} + V_{\theta 2}}{2} \right)^2 \right]^{1/2}, \tag{1}$$

where $V_{\mathrm{a1,2}}$ are axial velocities and $V_{\theta 1,2}$ are swirl velocities. The corresponding angle of the average flow is given by

$$\tan \beta_{\mathrm{m}} = \frac{1}{2} \left(\frac{V_{\theta 1}}{V_{\mathrm{a1}}} + \frac{V_{\theta 2}}{V_{\mathrm{a2}}} \right). \tag{2}$$

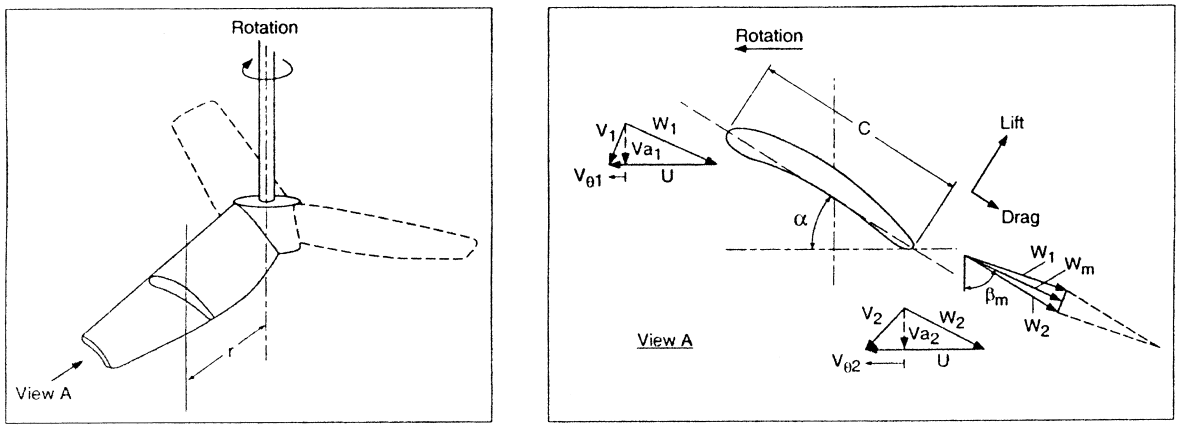

Fig. 2. Geometric details of blade element.

The lift and drag coefficients, C_L and C_D respectively, are related to the lift and drag forces per unit blade length (F_L and F_D) using the mean relative velocity W_m and the liquid density ρ

$$L = \frac{1}{2}\rho W_m^2 C_L c\,\mathrm{d}r, \qquad D = \frac{1}{2}\rho W_m^2 C_D c\,\mathrm{d}r. \tag{3}$$

The dimensionless lift and drag characteristics of the blade sections employed were established in a set of independent experiments as functions of the angle of attack γ where

$$\gamma = \alpha + \beta_m - \pi/2 \tag{4}$$

and α is the geometric angle of attack.

The total tangential force exerted by the blade section at radius r is

$$Y = N_b(F_L \cos\beta_m + F_D \sin\beta_m), \tag{5}$$

where N_b is the number of blades. Assuming that the integrated effect of the shear stresses on a boundary of the control volume containing the blade element is negligible, the total tangential force is equal to the rate of change of angular momentum

$$Y = \rho 2\pi r \mathrm{d}r(V_{a2}V_{\theta 2} - V_{a1}V_{\theta 1}). \tag{6}$$

Equating (5) and (6) and non-dimensionalising all parameters

$$\epsilon_{\theta 2} = \frac{\sigma}{2\cos\beta_m}\frac{(1+\Sigma)^2}{4}(C_L + C_D\tan\beta_m) + \epsilon_{\theta 1}, \tag{7}$$

$$\tan\beta_m = \frac{1/\lambda + (\epsilon_{\theta 1} + \epsilon_{\theta 2})/2}{(1+\Sigma)/2}, \tag{8}$$

where $\epsilon_{1,2} = V_{\theta 1,2}/\overline{V}_a$ is a swirl coefficient, $\sigma = cN_b/2\pi r$ is the blade solidity, $\Sigma = V_{a2}/\overline{V}_a$ is an axial velocity coefficient and $\lambda = \overline{V}_a/U$ is a flow coefficient, all based on the bulk axial velocity $\overline{V}_a = 4Q/\pi(D^2 - d^2)$, where Q is the volume flow rate through the impeller, D is the impeller diameter and d is the hub diameter. The bulk axial velocity $\overline{V}_a$ is assumed equal to V_{a1}.

3.1.2. Flow through the whole impeller

In the simulations to be described here, impeller flow radial velocities and $\epsilon_{\theta 1}$ (i.e., inlet swirl) were assumed to be zero and $\Sigma(r)$ (the radial distribution of impeller axial velocity) has been set using an experimentally established profile, as shown in Fig. 3. Given the bulk axial velocity $\overline{V}_a$,

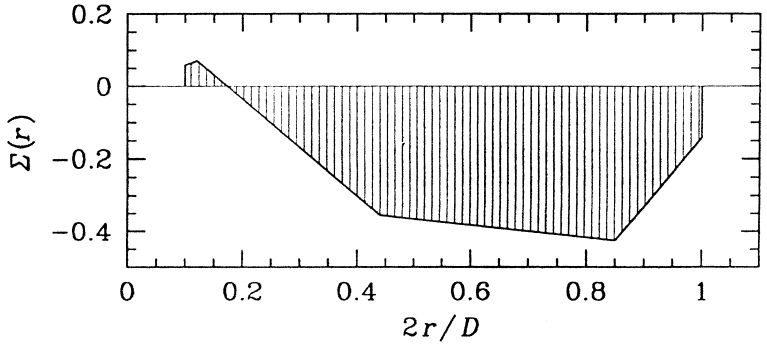

Fig. 3. Piecewise-linear impeller axial velocity distribution $\Sigma(r)$. The distribution was derived from typical experimental measurements of axial velocity beneath the impeller.

the functional relationships that describe $C_L(\beta_m)$, $C_D(\beta_m)$, together with (7) and (8) provide four equations in the four unknowns C_L, C_D, $\epsilon_{\theta 2}$ and β_m. At each radius, the equations are solved using a fixed point iteration scheme starting with an estimated value of β_m. Typically less than 10 iterations are required in order to achieve satisfactory convergence for the elemental impeller flows.

Descriptions of the impeller geometry, and curve fits to experimentally-derived values of lift and drag coefficients as functions of angle of attack for a typical blade section are maintained in look-up tables for access by the subroutine that calculates the flow through the impeller. The geometric data are given at a small number of radial positions (typically eight). Given the bulk axial flow rate through the impeller, the outlet swirl velocities are calculated at each of the radial positions and stored for interpolation onto the inflow boundary locations beneath the impeller in the CFD simulation of flow in the remainder of the tank. In this step it is assumed that the flow in the tank in the vicinity of the impeller is invariant in the azimuthal direction, i.e., that the inhomogeneity caused by the presence of the baffles has no localised effect on the flow through impeller.

3.2. CFD techniques

The tank flows have been simulated using a commercial block-structured finite-volume RANS solver, CFX-4.2 [1]. The block structure and a view of a typical quarter-tank computational mesh are shown in Fig. 4. The geometry of the mesh was arranged to match the tank-impeller combination used in the experiments. Periodic boundaries were employed on the azimuthal faces of the tank quadrant.

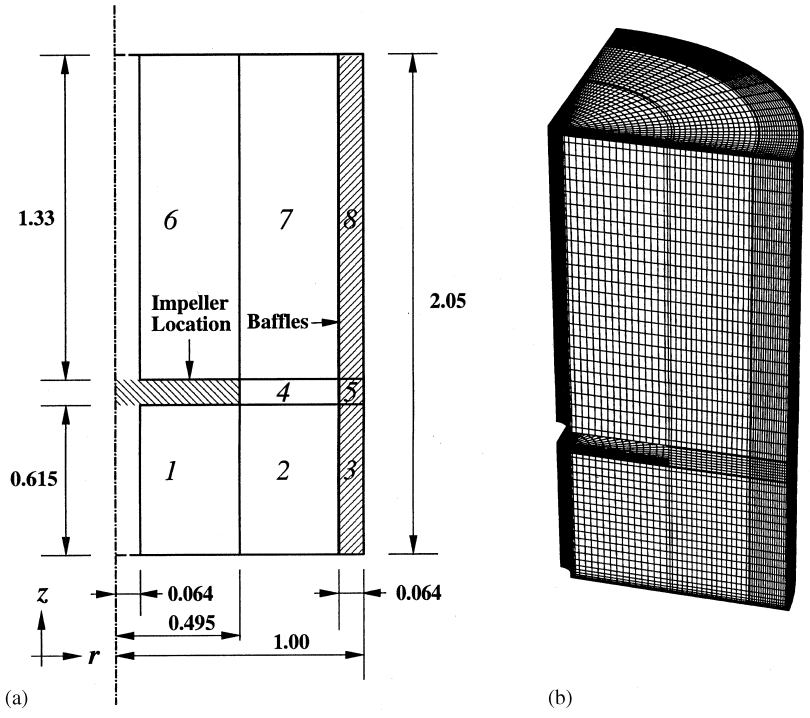

Fig. 4. Details of four-baffled mixing tank mesh: (a) block structure for tank mesh, dimensional information supplied in terms of tank radius; (b) associated 1/4-tank computational mesh, showing void region for impeller model; note the geometric progression of mesh spacing employed in the azimuthal direction in order to increase resolution near the baffles.

In the solver, the SIMPLEC iteration was used to implement the velocity–pressure coupling. An investigation of the use of different upwinding schemes and turbulence-model parameters for this problem has been presented in [6]. Second-order approximations were used for all terms in the discretised momentum equations including the advection terms, where the CCCT scheme [4,2] was used.

It has been found that for this flow a two-equation k–ε turbulence model produces satisfactory agreement with experimental results, probably because the presence of vertical baffles present in the mixing tanks acted to suppress strong swirl. A conventional wall-model treatment was employed to provide boundary conditions for the momentum equations at all solid surfaces, and a stress-free condition was used to represent the free surface of the liquid in the tank. Outflow boundary conditions were used above the impeller volume.

3.3. Rotor outflow turbulence characteristics

For the CFD simulation of flow in the tank, the region below the impeller is treated as an inlet boundary condition. While the impeller model allows the mean flow velocity field to be estimated it is unable to provide turbulence kinetic energy k and energy dissipation rate ε. It was found that reasonable estimates for these quantities were required for accurate simulation of the tank flows.

Through comparisons detailed in [6] it was established that an approximate estimate for the turbulence kinetic energy beneath the impeller was given by

$$k = 1.5I^2\overline{V}_{\mathrm{a}}^2, \tag{9}$$

where I is the turbulence intensity of the axial flow, with a typical measured value $I = 0.3$. This estimate assumes the turbulence to be isotropic. More accurate representations of k were tested but not found to significantly improve predictions. The value of ε at rotor outflow was estimated via a mixing-length approximation as

$$\varepsilon = k^{3/2}/l, \tag{10}$$

where a mixing length $l = 0.4D$ was used; the results were not sensitive to this assumption.

3.4. Convergence investigations

In order to examine the convergence properties of the flow simulation, tests were set up in which the number of mesh points was varied and the estimate of the amount of power dissipated in the tank was computed from the predictions of the turbulence model.

An integral estimate of the rate at which turbulence acts to convert mechanical energy to thermal energy by viscous dissipation is

$$P_{\mathrm{d}} = \int \rho\varepsilon \,\mathrm{d}V \simeq 4\rho \sum_{i=1}^{N} \varepsilon_i \Delta V_i, \tag{11}$$

where the integration is carried out over the tank volume and ε is the estimate of the local energy dissipation rate per unit mass in the CFD turbulence model. The discrete approximation uses the localised estimate of dissipation rate and volume of each cell, while the factor 4 accounts for the fact that the simulation represents a single quadrant of the complete tank volume. The additional viscous dissipation due the the mean flow shear rates was computed and found to be less than 1% of that due to the turbulence.

Table 1
Results of convergence study, showing power number N_P as a function of the number of finite volumes in a 1/4-tank mesh

No. of cells	12 360	51 420	119 000	127 160	189 440	310 100
N_P	0.3051	0.3253	0.3373	0.3410	0.3425	0.3435

In the convergence evaluations, the flow through the impeller region was set at a fixed value, and the power dissipation for the whole tank was approximated using (11). It was found that a geometric progression in the mesh spacing in the azimuthal direction, as shown in Fig. 4b, gave the most economical approximations, consistent with good resolution of flow details near the baffles. In addition, localised geometric refinements were used in the axial and radial directions near the tank walls.

Tabulated estimates of the power dissipation are shown in Table 1, where the power dissipation is given in dimensionless form

$$N_P = \frac{P_\mathrm{d}}{\rho N^3 D^5}. \tag{12}$$

It can be seen that the estimated power dissipation had converged to within 1% of the highest-resolution (310 100-cell) value at the 127 160-cell resolution, which was chosen for the remainder of the simulations. By way of visual comparison, the mesh shown in Fig. 4b corresponds to the 51 520-cell simulation.

3.5. Operating point

The operating point for the hybrid tank–impeller combination is set iteratively by adjusting the flow rate Q until the estimate of the power input to the tank computed using the impeller model matches the integral estimate of power dissipation in the tank computed from the turbulence model. The volume flow rate is obtained from the tank simulation by integrating the normal velocity component over the impeller inlet boundary.

By equating the incremental rate of change of angular momentum to the incremental torque exerted at each radial location, the maximum theoretical rise in total pressure head at radius r is

$$H(r) = \rho 2\pi N r (V_{\theta 2} - V_{\theta 1}). \tag{13}$$

The loss of pressure head due to blade drag is [3]

$$H_l(r) = \frac{1}{2}\rho \overline{V}_\mathrm{a}^2 C_\mathrm{D} \frac{\sigma(1+\Sigma)^2}{4\cos^3\beta_\mathrm{m}}, \tag{14}$$

and the blade efficiency at each radius

$$\eta(r) = \frac{H(r) - H_l(r)}{H(r)} \tag{15}$$

accounts for power transferred to the fluid within the control volume for the impeller element due to blade profile drag. The amount of power available to drive the tank flow can then be estimated from the blade element model as

$$P_i = Q \frac{\int_{d/2}^{D/2} \eta H \Sigma r \,\mathrm{d}r}{\int_{d/2}^{D/2} \Sigma r \,\mathrm{d}r}. \tag{16}$$

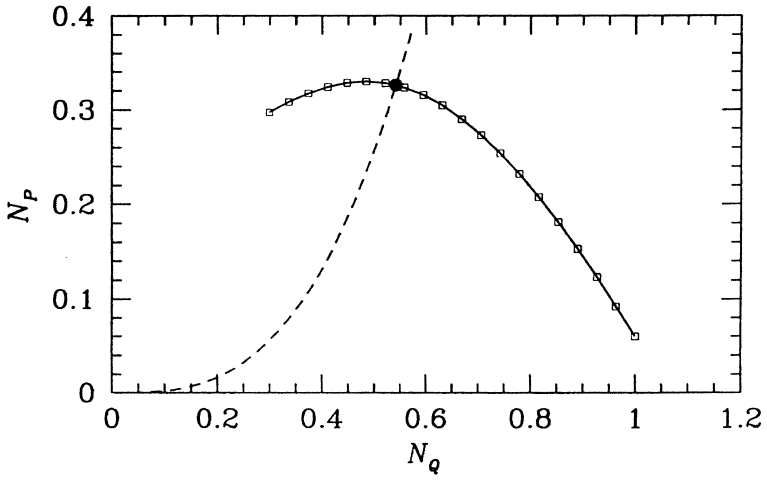

Fig. 5. Plot showing the estimated power delivery characteristic of the impeller N_{P_i} as a function of the dimensionless flowrate $N_Q = Q/ND^3$. The operating point and the assumed form of the tank power consumption characteristic are also shown.

The bulk performance characteristics of the impeller are calculated and stored in a pre-processing step which provides a look-up table of predicted rotor power delivery P_i for a number of bulk flow rates Q. For a fixed geometry and rotation rate N the operating point for the tank–impeller combination is set by adjusting Q (hence H and η) in a fixed-point iteration in order to equate P_i and P_d. In this iteration it is assumed that the tank losses P_d are locally a cubic function of Q, as appropriate for turbulent flow. The setting of the operating point occurs every 100 iterations of the CFD solution in the tank, forming a coupled iterative solution for the tank and rotor flows. This process continues until the operating point has converged. The assumed form of the tank power consumption curve is unimportant except in influencing the path taken through the convergence process. The estimated dimensionless operating characteristic of the impeller and the operating point obtained for the tank–impeller combination are shown in Fig. 5.

4. Results

4.1. Velocities

A comparison between experimental measurements of vertical-radial velocities and simulation results on the azimuthal mid-plane of the tank is shown in Fig. 6. For the comparison, the simulation results have been interpolated onto the same spatial locations as the experimental measurements. The qualitative and quantitative agreement between the two data sets is good. The general meridional flow is reproduced well by the simulation, including the region of reversed flow near the outer wall at the top of the tank. The average absolute deviation between the magnitudes of the in-plane velocities, normalised by the rotor tip speed, was 0.7%.

4.2. Operating point and power consumption

The predicted operating point for the impeller–tank combination, as shown in Fig. 5, was $N_Q = 0.54$, $N_P = 0.33$. This compares very favourably with experimental measurements [9], which gave $N_Q = 0.56$, $N_P = 0.33$ for the same impeller–tank combination. Isosurfaces of turbulent

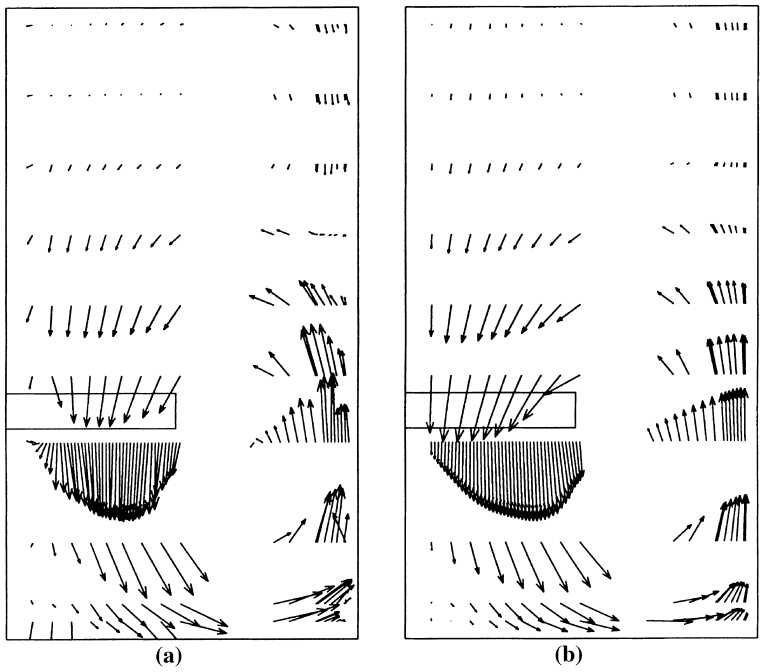

Fig. 6. Plot showing a comparison of (a) measured and (b) computed velocity vectors on the azimuthal mid-plane of the tank.

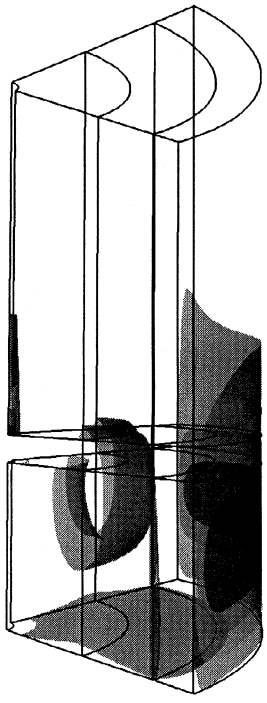

Fig. 7. Four isosurfaces of turbulent energy dissipation rate, ε. The highest dissipation rates occur near the outer wall of the tank, at elevations slightly less than that of the impeller.

energy dissipation, derived from the simulation, are shown in Fig. 7. The highest dissipation rates occur in the boundary layer on the tank wall at elevations slightly below that of the impeller.

5. Discussion and conclusions

The hybrid simulation method described here has been shown to produce simulation results of acceptable accuracy – typical velocity predictions were found to agree with experimental measurements to the order of 1% accuracy, as were power requirements. The method automatically balances estimates of power input and dissipation to predict the operating point for the impeller–tank combination. The technique allows rapid evaluation of alternative tank and rotor configurations. In particular, the effect of changing impeller geometric parameters (other than diameter), such as blade section and pitch, number of blades or blade chord, can be investigated without requiring remeshing of the tank domain. The method could readily be extended to deal with tanks with multiple axial flow impellers.

The technique requires information concerning impeller geometry and the lift–drag characteristics for the impeller blade section. Additionally, the radial distribution function of axial velocity through the impeller $\Sigma(r)$ must be nominated; in practice it has been found that the generalised shape illustrated in Fig. 3 provides a reasonable estimate for a wide range of impeller geometries. Finally, estimates of turbulence quantities k and ε must be supplied for the impeller outflow region, and guidelines for establishing appropriate values have been supplied in Section 3.3.

The method predicts only the time-average flow in the impeller–tank combination, and cannot simulate large-scale transient effects that may potentially be important in studies of mixing. However, since the model incorporates estimates for turbulence quantities, these can be used to provide estimates of shear rates for use in simulation of chemical reaction kinetics, particle aggregation/rupture etc., in process applications if desired.

The present hybrid approach is successful in part because of the well-developed theoretical understanding of flows through axial flow impellers. A time-averaged formulation is implicit in the present formulation of the hybrid scheme, both by adoption of RANS solution for the tank flows and azimuthal averaging of the impeller flows. It should be noted that the success of the assumption that azimuthally-averaged flow adequately represents the flow in the impeller region depends in part on the existence of a significant distance between the impeller tip and the tank baffles. In the present geometry, this distance was 45% of the impeller diameter, and it appears that the localised disruptions to the impeller flows caused by the baffles were comparatively unimportant with respect to the overall flow in the tank.

References

[1] AEA Technology, CFX-4.2: Solver, AEA Technology, UK, 1997.
[2] J.H. Alderton, N.S. Wilkes, Some applications of new finite difference schemes for fluid flow problems, Technical Report 13234, Atomic Energy Research Establishment, 1988.
[3] R.J. Downie, M.C. Thompson, R.A. Wallis, An engineering approach to blade designs for low to medium pressure rise rotor-only axial fans, Expt. Thermal Fluid Sci. 6 (1993) 376–401.
[4] P.H. Gaskell, A.K.C. Lau, An assessment of direct stress modelling for elliptic turbulent flows with the aid of a non-diffusive, boundedness-preserving discretization scheme, in: Conference on Numerical Methods Laminar and Turblent Flow, Montreal.
[5] A.D. Harvey, III, S.E. Rogers, Steady and unsteady computation of impeller-strirred reactors, A.I.Ch.E. J. 42 (10) (1996) 2701–2711.

[6] R.D. Niclasen, M. Rudman, H.M. Blackburn, J. Wu, Flow simulation of a mixing vessel incorporating blade element theory, in: Intnl Conf. Comput. Fluid Dyn. Mineral & Metals Proc. & Power Gen., CSIRO, Clayton, 1997, pp. 395–401.
[7] K.A. Pericleous, M.K. Patel, The modelling of tangential and axial agitators in chemical reactors, Physicochem. Hydrodyn. 8 (2) (1987) 105–123.
[8] R.A. Wallis, Axial Flow Fans and Ducts, Wiley, New York, 1983.
[9] J. Wu, L. Pullum, Performance analysis of axial flow mixing impellers, A.I.Ch.E.J. 46 (3) (2000) 289–498.